Dynamics and Metallicities of Red Supergiant Stars in the Young Massive Cluster NGC 2100

L. R. Patrick[1]⋆, C. J. Evans[1,2], B. Davies[3], et al.

[1] *Institute for Astronomy, University of Edinburgh, Royal Observatory Edinburgh, Blackford Hill, Edinburgh EH9 3HJ, UK*
[2] *UK Astronomy Technology Centre, Royal Observatory Edinburgh, Blackford Hill, Edinburgh EH9 3HJ, UK*
[3] *Astrophysics Research Institute, Liverpool John Moores University, Liverpool Science Park ic2, 146 Brownlow Hill, Liverpool L3 5RF, UK*

ABSTRACT
Studies of the dynamical state of young massive clusters can distinguish between models of early-time evolution. We have obtained KMOS near-IR spectroscopy for 14 red supergiant stars in the young massive star cluster NGC 2100 in the Large Magellanic Cloud (LMC). Radial velocities are estimated for the targets and the dynamical properties are estimated for the first time within this cluster. The line-of-sight velocity dispersion is shown to be flat outside of 10 pc from the cluster centre and is estimated to be $\sigma_{1D} = 2.4 \pm 0.4\,\mathrm{km\,s^{-1}}$. The dynamical mass of the cluster is derived as $log(M_{dyn}/M_\odot) > 4.8$ assuming virial equilibrium. Comparing this to the mass estimated using photometry we find the dynamical mass to be a factor of five smaller.

Stellar parameters including metallicity are estimated using the J-band analysis technique which has been rigorously tested in the Local Universe. The results of this analysis are shown to compare well with previous metallicity estimates within this cluster and to within the LMC in general. The age of the NGC 2100 is estimated to be $20 \pm 5\,\mathrm{Myr}$ using isochrone fitting to the RSG population, in good agreement with previous estimates.

Key words: Red Supegiants: stars. Clusters: NGC 2100. Galaxy: LMC.

1 INTRODUCTION

Globular clusters (GCs) were until recently thought to consist of a simple stellar population where all of the stars within the cluster were formed from in one homogeneous star forming burst. Recent results have thrown this traditional view into contention and many GCs have been shown to display features like an extended main-sequence turn off, double main sequences, as well as distinct chemical and dynamical populations. The most accepted method to explain these observations is to evoke a GC with multiple stellar populations.

Young massive clusters are important probes of cluster evolution. These custers have gained considerable attention within the past 20 years as tracers of star formation (e.g. Whitmore & Schweizer 1995; Miller et al. 1997; Zepf et al. 1999). Young massive clusters are thought to be younger counterparts to Globular Clusters. Recently, GCs have been proposed to contain multiple stellar populations based on their kinematics, metallicities and main sequence turn-offs. Studying young massive clusters can help to constrain some of the proposed models for creating multiple stellar populations within GCs.

Niederhofer et al. (2015), show that there exists no significant age spread in several young massive clusters within the LMC. In recent years it has become clear that young massive clusters appear to remain in virial equilibrium from an early stage (Longmore et al. 2014). This is in direct conflict with the formation scenario where star clusters are destroyed owing to gas expulsion (i.e. infant mortality, Lada & Lada 2003).

Over the last few years, medium resolution ($R > 3000$) near-IR spectroscopy has been shown to be a powerful tool to estimate stellar parameters for red supergiant stars (RSGs; Davies et al. 2010). This technique has been tested rigourousness by Gazak et al. (2014) and Davies et al. (2015) and demonstrated with data from the K-band multi-object spectrograph first in Patrick et al. (2015) who investigated the metallicity distribution within NGC 6822 ($d = 0.5\,Mpc$) then by Gazak et al. (2015) who compare the metallicity gradient derived within NGC 300, a grand design spiral galaxy outside the Local Group ($d = 1.9\,Mpc$), finding striking agreement with blue supergiant stars (BSGs).

Using multi-object spectrographs like KMOS to observe RSGs provides an efficient way to construct a sample of

⋆ E-mail: lrp@roe.ac.uk

metallicity measurements in extragalactic stellar systems where one can study the distribution and build-up of metals within these systems.

NGC 2100 is a young massive cluster in the Large Magellanic Cloud (LMC), located near the large star forming region 30 Doradus. With an age of $\sim$20 Myr (Elson 1991; Niederhofer et al. 2015), and a mass of $4.6 \times 10^4 M_\odot$ (McLaughlin & van der Marel 2005, assuming King (1966) profiles), NGC 2100 falls within the mass and age range where the infrared cluster light is dominated by RSGs (Gazak et al. 2013). This has been confirmed observationally where a large number of RSGs have been identified within this cluster.

NGC 2100 is not a cluster in isolation. It is located in one of the most actively star-forming regions within the Local Group of galaxies. At $\sim$20 Myr old, the most massive members of this star cluster have already gone supernova. This has had a profound affect on the surrounding gas and dust, and has potentially shaped the surrounding LMC 2 supershell (see Points et al. 1999).

In this study we estimate stellar parameters from KMOS spectroscopy for 14 RSGs in the vicinity of the young massive cluster NGC 2100. Section 2 we describe the observations and data reduction, and in section 3 we detail our results, focusing on radial velocities of the target stars where we derive the line-of-sight velocity dispersion, the dynamical mass of NGC 2100 and the stellar parameters. Our results are discussed in Section 4 and conclusions are presented in Section 5.

2   OBSERVATIONS AND DATA REDUCTION

2.1   Target Selection

- Ben, could you write a few lines here?

2.2   KMOS Observations

These observations form part of the KMOS Guaranteed Time Observing (PI: Evans) and were conducted in March 2015. The observations consist of 8×10 s exposures taken with the YJ grating with sky offset exposures (S) interleaved between the object (O) exposures in an O, S, O observing pattern. In addition, a standard set of KMOS calibrate frames were also obtained as well as telluric standard frames using HD 51506 as the telluric standard star. Seeing conditions were stable at 1.0 arcseconds for the course of the observations.

The KMOS/esorex standard routines (SPARK; Davies et al. 2013) were used to calibrate and reconstruct the data cubes. Telluric correction was performed using the 24-arm telluric correction routine (described in detail by Patrick et al. 2015). Briefly, corrections to the standard telluric recipe are put in place to correct for slight differences in wavelength calibration between the telluric and science spectra. This is implemented using an iterative cross-correlation approach. Additionally, differences in the strength of the telluric features are corrected by apply a simple scaling using the equation,
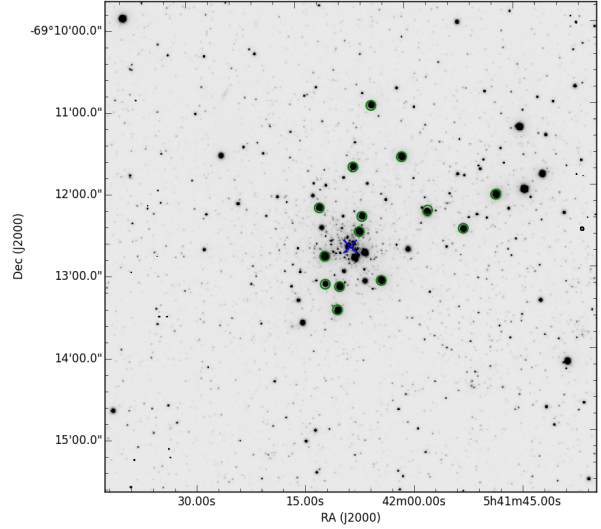

Figure 1. Positions of the NGC 2100 KMOS targets overlaid on a VISTA *J*-band image. Green circles indicate KMOS targets. The cluster centre has been marked by a small blue cross. **include 5pc marker!**

$$T_2 = (T_1 + c)/(1 + c) \qquad (1)$$

where T_2 is the scaled telluric-standard spectrum, T_1 is the uncorrected telluric-standard spectrum and c is the scaling parameter which is varied from $c = -0.5$ to $c = 0.5$ in increments of 0.02. The best c value is chosen based on the overall standard deviation of the spectrum, i.e. the c value producing the smallest σ is selected. Once these corrections are accounted for, the science spectra are divided by the appropriate telluric spectrum for that particular IFU.

3   RESULTS

3.1   Radial velocities

Radial velocities are estimated using an iterative cross-correlation method. To ensure systematic shifts are removed, the observed spectra are first cross-correlated against a spectrum of the Earth's atmosphere, taken from the ISAAC webpages, which is at a much higher resolution than that of the KMOS observations. This cross-correlation is performed in the $1.15 - 1.17\,\mu$m region as this is where the telluric features dominate. This shift is then applied to the $1.16 - 1.22\,\mu$m region, i.e. where the radial velocity is estimated.

Once the observed spectra are on a consistent wavelength solution, an initial guess of the radial velocity is estimated by cross-correlating the science spectra with an appropriate synthetic RSG spectrum in the $1.17 - 1.21\,\mu$m region. This wavelength regime is selected based on the dominance of atomic features in the RSG spectrum at these wavelengths. To increase reliability, this initial guess is improved upon by using five carefully selected groups of stellar absorption lines centred on some of the strongest atomic features

Table 1. Summary of VLT-KMOS targets in NGC 2100.

ID	S/N	α (J2000)	δ (J2000)	B	V	I	J	H	K_s	RV (km s^{-1})	Notes
0207-0134568	318	05:41:47.873	-69:12:05.959	16.488	13.749	9.769	9.525	8.603	8.200	238.9±1.1	
0207-0134683	198	05:41:52.430	-69:12:30.410	16.430	14.267	11.970	10.413	9.526	9.155	238.7±2.2	
0207-0134811	202	05:41:57.286	-69:12:16.480	14.074	13.019	11.170	9.811	9.036	8.738	239.8±1.3	C2
0207-0134979	252	05:42:03.877	-69:13:07.410	15.624	13.579	11.410	9.839	8.996	8.740	240.4±1.5	
0207-0135059	196	05:42:06.348	-69:12:20.150	00.000	00.000	11.810	10.371	9.480	9.159	245.0±2.9	B17
0207-0135069	256	05:42:06.764	-69:12:31.245	15.643	13.675	11.390	9.977	9.150	8.807	239.5±2.3	
0207-0135150	240	05:42:09.647	-69:13:11.263	15.367	13.383	11.370	9.976	9.136	8.841	240.8±3.2	
0207-0135162	250	05:42:10.001	-69:13:28.210	16.060	13.827	11.580	10.021	9.150	8.823	240.2±1.4	C32
0207-0135205	304	05:42:11.574	-69:12:48.770	16.327	14.033	11.450	9.557	8.617	8.264	238.0±1.9	
0207-0135206	151	05:42:11.592	-69:13:09.257	16.165	14.272	12.340	10.943	10.090	9.788	241.4±2.5	
0207-0135220	195	05:42:12.182	-69:12:13.144	15.483	13.606	11.750	10.440	9.622	9.335	246.0±3.3	
0208-0135292	262	05:42:00.722	-69:11:36.925	15.579	13.674	9.421	9.900	9.017	8.683	242.2±3.1	
0208-0135383	211	05:42:04.762	-69:10:58.816	15.550	13.800	12.770	10.319	9.427	9.159	245.7±2.3	
0208-0135446	201	05:42:07.435	-69:11:43.692	15.531	13.661	11.780	10.482	9.610	9.351	242.4±3.2	

Photometric data taken from the SIMBAD database. Typical errors on photometric data: 0.026, 0.014, 0.04, 0.024, 0.026, 0.022 respectively. Near-IR data taken from 2MASS.

in this region. These lines and regions are selected based on their reliability and are known to be not affected by telluric absorption. Figure 2 illustrates the selected features used for the analysis.

Radial velocities are independently calculated for each region by means of iterative cross-correlation. This results in five estimates of the radial velocity for each star which are then compared and any region which produces a radial velocity which is an obvious outlier to the distribution is rejected. The final radial velocity for each star is the mean of the distribution resulting from the (non-rejected) regions. Not rejecting these outliers has the effect of increasing the error on each individual radial velocity but it does not alter the mean of the sample or the deviation significantly ($< RV > = 244 \pm 3$ km s^{-1}). The error on this mean is calculated by taking the standard deviation of the data, normalised by the number of regions used ($err = \sigma/N_{regions}$). This method is known to work well for KMOS spectra (Lapenna et al. 2015; Patrick et al. 2015).

Figure 3 shows all stellar radial velocitiy estimates as a function of distance from the centre of the cluster, alongside the systemic radial velocity of the LMC (green dashed line). Given the low dispersion of the radial velocity measurments for the KMOS targets, we confirm that all of the targets within this sample are members of NGC 2100. Table 2 details previous measurements of radial velocities within this cluster.

Recently, Evans et al. (2015) used AAOmega to measure radial velocities of massive stars within LMC, which included two sources in NGC 2100: star 407 (O9.5 II 258.5 ± 3.4 km s^{-1}) and star 408 (B3 Ia; 250.6 ± 1.3 km s^{-1}).

Jasniewicz & Thevenin (1994) measure radial velocities for four RSGs in NGC 2100 (B17, C2, C32 and C34 using the nomenclature of Robertson 1974). Three of these stars have been observed with KMOS in the present study (207-0135059; B17, 207-0134811; C2 and 207-0135162; C32). A comparison between the radial velocities estimated in JT94 with those presented here highlight the discrepancy between the velocities estimated in this study. The average offset between the three stars which are common to the samples is -18.3 ± 5.2 km s^{-1}. However, previous stellar radial velocity estimates using KMOS have shown a small, not-statistically significant offsets when compared with previous measurements (Lapenna et al. 2015; Patrick et al. 2015). Regardless,
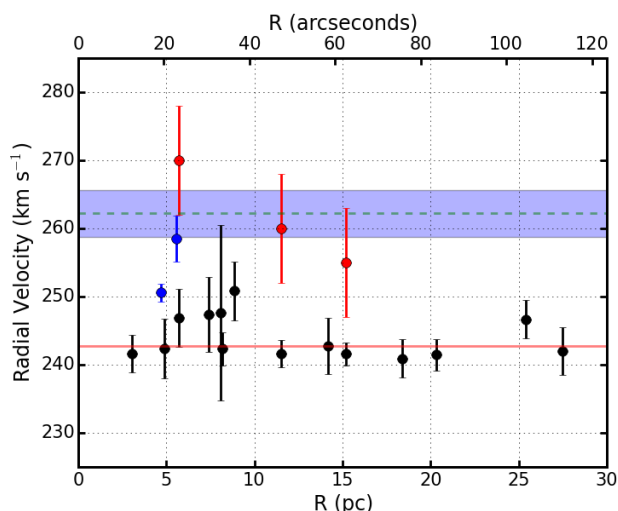

Figure 3. Radial velocities of KMOS targets shown as a function of distance from the cluster centre. Green dashed line shows the LMC systemtic veloctiy with the error highlighed by the blue shaded region (262.2 ± 3.4 km s^{-1}; McConnachie 2012) and the solid red line shows the mean of the sample (242.7 ± 2.4 km s^{-1}). Blue points show the two young stars studied in Evans et al. (2015) and red points show previous esimates for three of the targets (Jasniewicz & Thevenin 1994).

we can not ignore the possibility that there exists some systematic offset in the radial velocity measurements estimated in this study.

Freeman et al. (1983) compile integrated light radial velocities from Andrews & Lloyd Evans (1972) and Ford (1970) to define an average of 267 ± 13 km s^{-1}. Whereas Smith & Weedman (1971), measure the radial velocity of the HII gas of NGC 2100 as 282.2 ± 2.5 km s^{-1}.

3.2   Velocity Dispersion

An upper limit to the line-of-sight velocity dispersion is calculated using the equations,

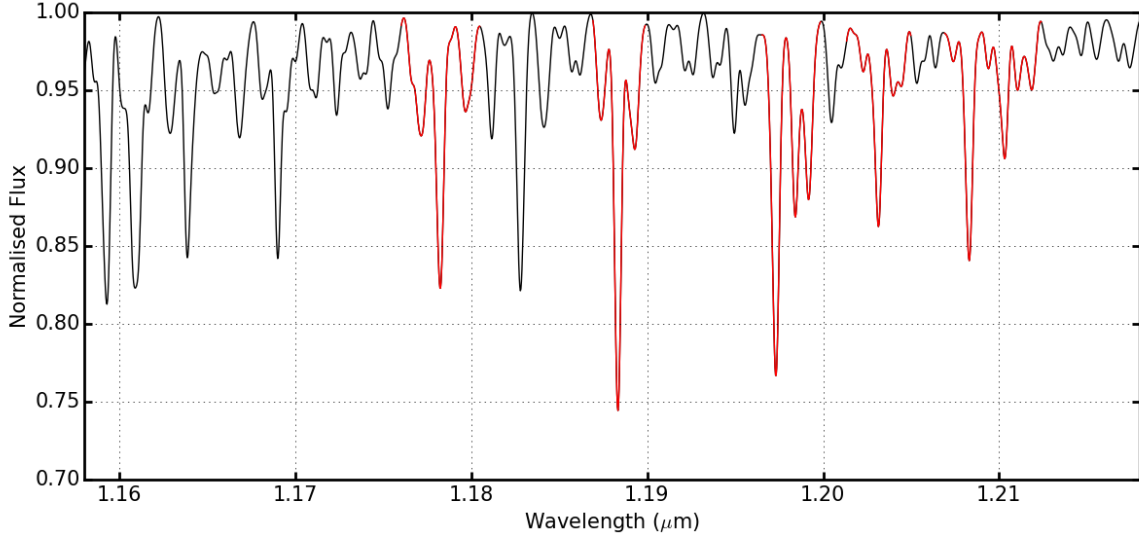$$\mu = \frac{1}{\sum_i 1/\sigma_i^2} \sum_i \frac{RV_i}{\sigma_i}, \qquad (2)$$

Figure 2. Sythetic RSG spectrum used calcualte the radial velocities for programme stars. Red regions illustrate regions where a cross-correlation is performed between the observed spectra and this synthetic spectrum. These regions provide consistent results with an average dispersion between the five regions of of $2.3 \, \text{km s}^{-1}$.

Table 2. Previous radial velocity measurements in NGC 2100.

ID	ID in current study	RV (km s^{-1})	Reference	Notes
407	—	258.5 ± 3.4	Evans et al. (2015)	O9.5 II
408	—	250.6 ± 1.3	Evans et al. (2015)	B3 Ia
B17	207-0135059	$255 \pm 8/245.0 \pm 2.9$	Jasniewicz & Thevenin (1994)	
C2	207-0134811	$270 \pm 8/239.8 \pm 1.3$	Jasniewicz & Thevenin (1994)	
C32	207-0135162	$260 \pm 8/240.2 \pm 1.4$	Jasniewicz & Thevenin (1994)	
C34	—	265 ± 8	Jasniewicz & Thevenin (1994)	
NGC 2100	—	$280 \pm 10(16)$	Andrews & Lloyd Evans (1972)	Whole cluster
NGC 2100	—	282.2 ± 2.5	Smith & Weedman (1971)	Gas
NGC 2100	—	253 ± 17	Ford (1970)	

Value in braces is the error defined from Freeman et al. (1983).

$$Var = \frac{1}{\sum_i 1/\sigma_i^2} \sum_i \frac{(RV_i - \mu)^2}{\sigma_i^2}, \qquad (3)$$

$$\sigma_{1D} = \sqrt{Var \frac{N}{N-1}}, \qquad (4)$$

where σ_i is the uncertainty on the radial velocity measurement RV_i, μ is the weighted mean and N is the number of stars in the sample. Figure 4 shows the line-of-sight velocity dispersion profile for RSGs in NGC 2100. We see that the dispersion is consistent with a flat profile with a value of $\sim2.5 \, \text{km s}^{-1}$. The apparent outlier at $\sim5 \, \text{pc}$ is owing to the low number statistics within this radius. Thus, we adopt $\sigma_{1D} = 2.4 \pm 0.4 \, \text{km s}^{-1}$, where the error is the average error σ_{1D} measurements of the sample, as an upper limit on the line-of-sight velocity dispersion profile of NGC 2100. A discussion on how binarity affects this distribution is given in Section 4.2.
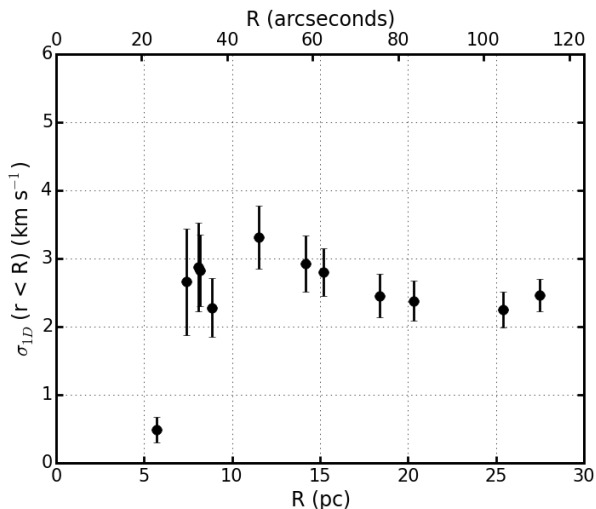
3.3 Dynamical Mass

Using σ_{1D} as an upper limit on the velocity distribution, one can calculate the dynamical mass of the cluster using the virial equation,

$$M_{dyn} = \frac{\eta \sigma_{1D}^2 r_{eff}}{G}, \qquad (5)$$

where M_{dyn} is the virial mass, $\eta = 6r_{vir}/r_{eff} = 9.75$ providing the density profile of the cluster is sufficiently steep (Portegies Zwart et al. 2010). However, NGC 2100 has a relatively shallow density profile ($\gamma = 2.3$) which means $\eta > 9.75$ therefore the estimate of M_{dyn} is knowingly an overestimate. Using $\sigma_{1D} = 2.4 \pm 0.4 \, \text{km s}^{-1}$ and equation 5, the dynamical mass of NGC 2100 is $M_{dyn} = (5.8 \pm 2.0) \times 10^4 M_\odot$. Comparing this to the photometric mass $M_{phot} = (2.3 \pm 1.0) \times 10^4 M_\odot$ (McLaughlin & van der Marel 2005) we see that the dynamical mass appears to be a barely significant overestimate. Gieles et al. (2010) explain this discrepancy by demonstrating that binary motions can increase the measured velocity dispersion profile. Hénault-Brunet et al. (2012) note that had binarity been neglected they would have measured a σ_{1D} a factor of five higher for R136. How-

Figure 4. Observed line-of-sight velocity dispersion as a function of the distance from the centre of NGC 2100.

Figure 6. Estimated metallicities shown against distance from the centre of the cluster where the solid blue line denotes the mean of the sample $-0.3 \pm 0.11\,dex$.

Table 3. Model grid used for analysis.

Model Parameter	Min.	Max.	Step size
T_{eff} (K)	3400	4400	100
[Z] (dex)	-1.0	1.0	0.1
$\log g$ (cgs)	-1.00	1.00	0.25
ξ (km s^{-1})	1.0	5.0	0.2

ever, the mean lifetime for RSGs within binary systems is significantly decreased (Eldridge et al. 2008). These authors also note that where mass transfer occurs, the number of RSGs drastically decreases. We can therefore expect that the numbers of RSGs in a close binary system are very small Davies et al. (2009).

Therefore, the velocity dispersion profile derived using an effectively single sample of RSGs should not be affected by binary motions. This leads to the conclusion that the only factor affecting the estimation of M_{dyn} is the η parameter. Using a lower limit of $\eta = 7.0$ (estimated from Fig. 4a from Portegies Zwart et al. 2010), $M_{dyn} = (4.2 \pm 1.4) \times 10^4 M_\odot$ which still lies above the photometric mass however with a low significance. Why this is the case is addressed in section 4.

3.4 Stellar Parameters

Stellar parameters are estimated using the J-band analysis technique described initially in Davies et al. (2010) and tested rigorously in Gazak et al. (2014) and Davies et al. (2015). These studies show that using a narrow spectral window within the *J*-band one can accurately derive global metallicity ([Z]) to within $\pm 0.2\,dex$ at the resolution of KMOS observations with S/N $\geqslant$ 100. Patrick et al. (2015) builds on this by demonstrating the feasibility of this technique using KMOS spectra.

This analysis uses synthetic RSG spectra, extracted from MARCS model atmospheres (Gustafsson et al. 2008), computed with non-local thermodynamic equilibrium corrections for stellar lines for titanium, iron, silicon and magnesium (Bergemann et al. 2012, 2013, 2015). The parameter ranges for the grid of synthetic RSG spectra are listed in Table 3. The synthetic spectra are compared with observations using a χ-squared minimisation approach where the synthetic spectra are degraded to the resolution and sampling of the observations.

Estimated stellar parameters are listed in Table 4. Reliable parameters could not be estimated for two stars (0207-0135059 and 0207-0135206). Figure 5 shows the observed
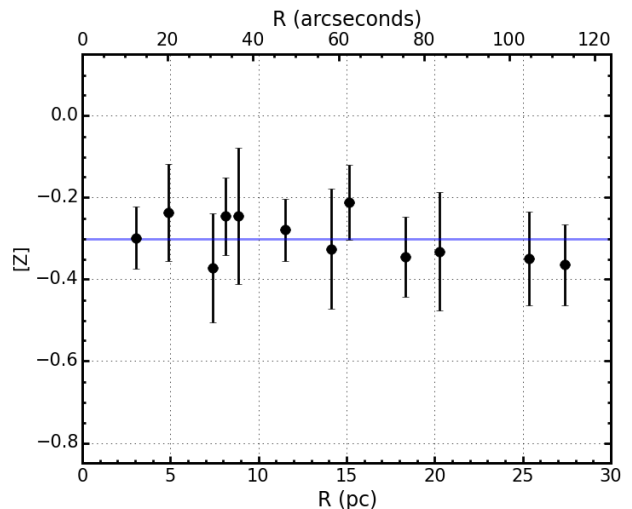
KMOS spectra (black) along with each best-fitting model spectrum (red). The average metallicity for the 11 stars within NGC 2100 is $-0.30 \pm 0.11\,dex$ and the distribution of metals with respect to distance from the cluster centre is shown in Figure 6. This figure shown no evidence for a spatial distribution of metallicity across the extent of the cluster.

The average metallicity in NGC 2100 compares well to estimates of the cluster metallicity using isochrone fitting to the optical colour-magnitude diagram ($-0.34\,dex$; Niederhofer et al. 2015). The only other estimate of stellar metallicity within this cluster comes from Jasniewicz & Thevenin (1994) who estimate metallicities using optical spectroscopy of four RSGs. This study finds an average metallicity for NGC 2100 $-0.32 \pm 0.03\,dex$ which our estimate agrees well with.

Using the same analysis technique as used in this study, Davies et al. (2015) estimate metallicities for nine RSGs within the LMC, finding an average value of $-0.37 \pm 0.14\,dex$ which again, our estimate agrees well with.

4 DISCUSSION

4.1 Stellar Parameters

As mentioned previously, JT94 measure stellar parameters for four RSGs using optical spectroscopy. These authors measure effective temperature, surface gravity and metallicity for each star by comparing their spectra to a set of synthetic spectra. A method not dissimilar to our own. We
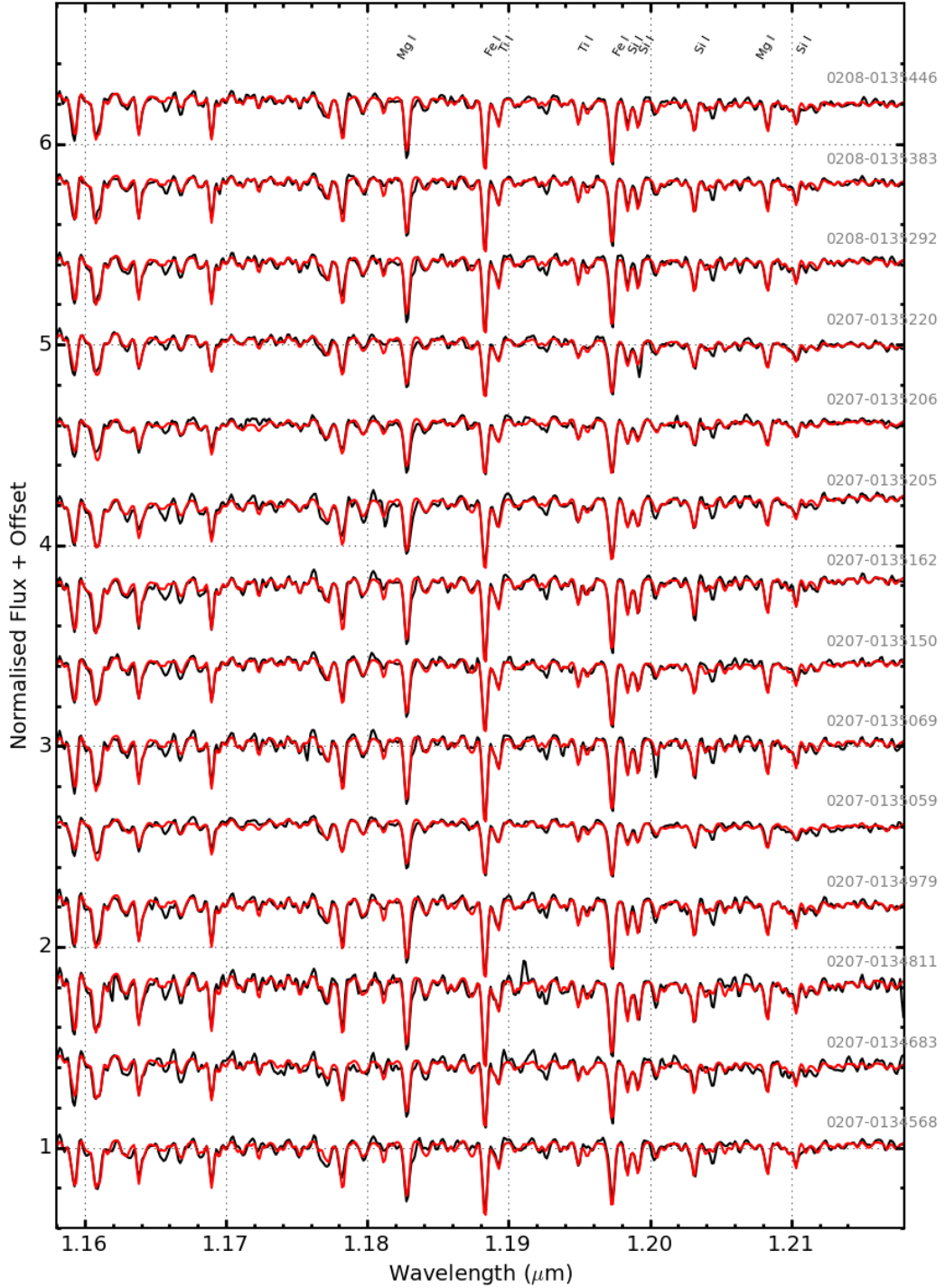
Figure 5. KMOS spectra of the NGC 2100 RSGs and their associated best-fit model spectra (black and red lines, respectively). The lines used for the analysis from left-to-right by species are: Fe I$\lambda\lambda$1.188285, 1.197305, Si I$\lambda\lambda$1.198419, 1.199157, 1.203151, 1.210353, Ti I$\lambda\lambda$1.189289, 1.194954.

Table 4. Fit parameters for NGC 2100 KMOS targets

Target	IFU	ξ (km s^{-1})	[Z]	$\log g$	T$_{eff}$ (K)	Notes
0207-0134568	7	3.8 ± 0.3	-0.36 ± 0.10	0.50 ± 0.09	4017 ± 55	
0207-0134683	9	3.6 ± 0.3	-0.33 ± 0.15	0.96 ± 0.38	4100 ± 71	
0207-0134811	6	5.0 ± 0.1	-0.21 ± 0.09	0.67 ± 0.17	4084 ± 47	C2
0207-0134979	12	4.4 ± 0.3	-0.25 ± 0.10	0.74 ± 0.12	4000 ± 31	
0207-0135059	24	2.2 ± 0.8	0.32 ± 0.42	0.85 ± 0.11	3715 ± 181	B17
0207-0135069	10	4.9 ± 0.1	-0.30 ± 0.08	0.70 ± 0.12	4013 ± 37	
0207-0135150	14	4.1 ± 0.3	-0.37 ± 0.13	0.73 ± 0.14	3900 ± 57	
0207-0135162	11	5.0 ± 0.1	-0.28 ± 0.08	0.70 ± 0.19	4024 ± 43	C32
0207-0135205	20	4.2 ± 0.3	-0.24 ± 0.12	0.50 ± 0.09	3896 ± 61	
0207-0135206	18	2.0 ± 0.4	0.56 ± 0.23	1.00 ± 0.00	3671 ± 104	
0207-0135220	22	3.6 ± 0.4	-0.24 ± 0.17	1.00 ± 0.12	4034 ± 50	
0208-0135292	4	4.3 ± 0.3	-0.34 ± 0.10	0.75 ± 0.10	3947 ± 50	
0208-0135383	3	4.2 ± 0.3	-0.35 ± 0.11	0.91 ± 0.16	3965 ± 50	
0208-0135446	2	4.1 ± 0.3	-0.33 ± 0.15	0.97 ± 0.11	3911 ± 67	

find that there are three targets in common with our study: B17, C2, C32 (using the Robertson 1974, nomenclature). **Comparing results we find B17 has a spuriously high metallicity for the sample. However, this spectrum displays no obvious features of a poor telluric correction or sky subtraction with a signal-to-noise ratio far exceeding that of our minimum threshold to perform the analysis. C34 & C2 have a microturblence value on the edge of the grid.**

When we compare the average values taken from JT94 we find excellent agreement for all parameters.

Luminosities have been estimated using the bolometric correction in Davies et al. (2013) and a H-R diagram for the clusters is presented in Figure 7. Overlaid on this H-R diagram are SYCLIST stellar isochrones for both SMC-like (solid lines Georgy et al. 2013) and solar-like (dashed lines) at various ages where stellar rotation is 40% of break-up velocity. Even though the temperatures covered by the SMC-like models do not accurately represent the distribution of temperatures observed in this study, it remains useful to fit the data using these models to estimate an age of NGC 2100. The Solar-like models (grey) demonstrate that increasing the metallicity of the sample a) decreased the temperatures of the RSGs (something which is not observed in Patrick et al. 2015), b) induces a blue-ward evolution for the youngest models and c) increases the luminosity for the oldest models.

Davies et al. (2015) estimate stellar parameters for nine RSGs throughout the LMC using the same methodology as that used in this study. In Figure 9 we compare the effective temperatures and metallicities from NGC 2100 with those derived for RSGs within the whole LMC. We find excellent agreement in the distribution of temperatures from the two studies, with the average agreeing well. The range in [Z] from the LMC population is slightly larger than that of the NGC 2100 RSGs, which is expected when comparing a star cluster with an entire galaxy, however the averages for the two studies agree very well.

4.2 Velocity Dispersion and Dynamical Mass

This study represents the first estimate of the line-of-sight velocity dispersion profile for NGC 2100. Comparing this estimate with that of other young massive clusters in the Local Universe is useful to ascertain whether this cluster shares similar properties to other more well studied young massive
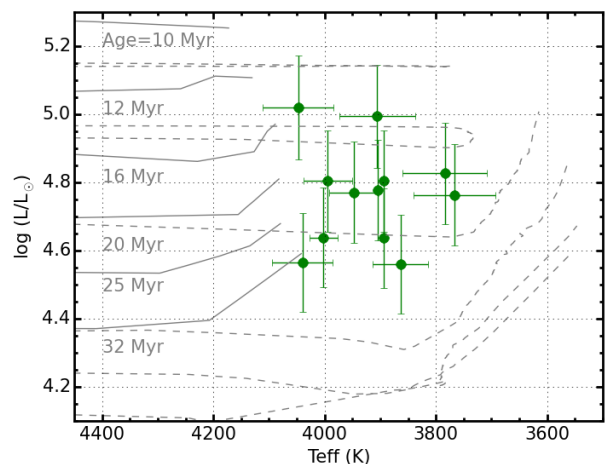
Figure 7. H-R diagram for 12 RSGs in NGC2100. Bolometric corrections computed using Davies et al. (2013). Cluster isochrones for solar (dashed lines Ekström et al. 2012) and smc-like (solid lines Georgy et al. 2013) metal abundances, where stellar rotation is 40% of the break-up velocity, are shown for ages of 10-32 Myr.

clusters. We find the dynamical properties NGC 2100 is well matched by other clusters with similar masses and ages, particularly so with RSGC02, a Galactic young massive cluster. Below we compare the dynamical results for NGC 2100 to that of several young massive clusters first within the LMC and then within the Galaxy. A comparison with a small sample of Local Group clusters reveals the trend that younger clusters have a larger line-of-sight velocity which relaxes to ~3 km s^{-1} at 10-100 Myr.

4.2.1 Comparison with LMC clusters

The line-of-sight velocity dispersion profile of the young massive cluster R136 has been estimated at 6 km s^{-1} (Hénault-Brunet et al. 2012) using multi-epoch spectroscopy from the VLT-Flames Tarantula Survey (Evans et al. 2011). NGC 2100 and R136 are both located within the 30 Doradus region and within the LMC 2 supershell. R136 is around twice as massive as NGC 2100 with the photometric mass of R136 being estimated at ~ $10^5 M_\odot$ with an age
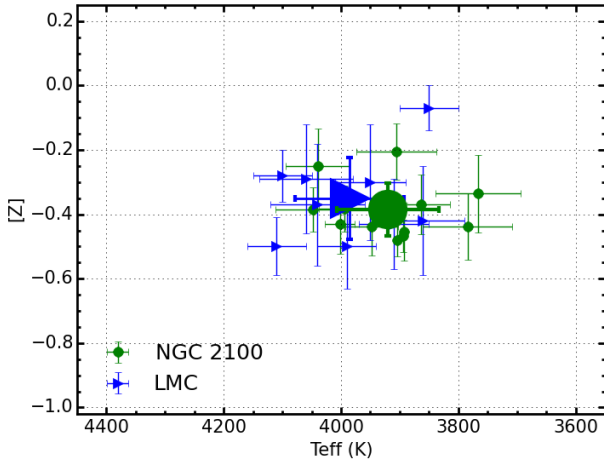
Figure 8. Estimated metallicities for NGC 2100 RSGs in this study shown against effective temperature (green dots). For comparison we show the distribution of LMC RSGs in Davies et al. (blue triangles 2015). This demonstrates the remarkable agreement between the effective temperature ranges and averages for RSGs within these two samples.
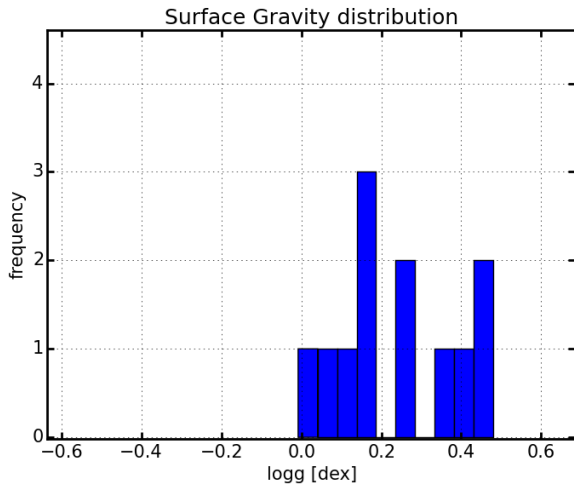

Figure 9. Histogram showing the range of surface gravities estimated. Average value $0.24 \pm 0.15\,dex$. For Illustration only.

less than 2 Myr (de Koter et al. 1998; Massey & Hunter 1998; Crowther et al. 2010). This makes R136 significantly younger than NGC 2100 (~ 20 Myr) and it is therefore unsurprising that the velocity dispersion profile is larger for R136 as one would expect a massive cluster to relax over time.

NGC 1850 is a young LMC massive cluster with a photometric mass of 1.4×10^5 and a recently revised age of 93 Myr (Niederhofer et al. 2015). McLaughlin & van der Marel (2005) report a line-of-sight velocity dispersion for this cluster as 3.0 ± 0.7 km s^{-1}which compares well to the dispersion in NGC 2100 even though this cluster is significantly older and more massive.

NGC 2004 is a young massive cluster in the LMC with a mass and age similar to that of NGC 2100 (20 Myr;

$2 \times 10^4 M_\odot$ Niederhofer et al. 2015, and references therein). Evans et al. (2006) obtained multi-epoch spectra for massive stars within this cluster and derive radial velocities without however a dynamical analysis of the cluster. This cluster has remarkably similar properties to NGC 2100 and therefore a comparison between their dynamical properties is useful to investigate the intrinsic distribution of dynamical properties within young massive clusters. However, this is beyond the scope of the current study.

4.2.2   Comparison with Galactic Clusters

RSGC01 is a cluster with a large population of RSGs within the Galaxy (Davies et al. 2007). This cluster is shown to have a mass $\sim 3 \times 10^4 M_\odot$ with an age 17 Myr and a velocity dispersion of 2.8 km s^{-1}. Therefore this cluster compares remarkably well with the properties of NGC 2100.

Westerlund 1 is a massive young star cluster in the Galaxy with a large population of massive stars (Clark et al. 2005). This cluster is young compared to NGC 2100 with an age of 3.5 Myr therefore many of the stars which will become RSGs in the future are currently fusing hydrogen on the main sequence. The photometric mass of Westerlund 1 is $\sim 3 \times 10^4 M_\odot$ with a measured velocity dispersion of 5.8 km s^{-1}. Like R136 in the LMC, Westerlund 1 has a higher velocity dispersion and a young age.

5   CONCLUSIONS

Using KMOS spectra of 14 RSGs in NGC 2100 we have for the fist time estimated the dynamical properties of this young massive cluster. Radial velocities have been estimated using KMOS, to a precision of ~ 1 km s^{-1}, demonstrating that this instrument can be used to study the dynamical properties of star clusters in external galaxies.

The line-of-sight velocity dispersion profile has been estimated in Figure 4 and has been shown to be flat outside 10 pc from the cluster centre. A low velocity dispersion of $\sigma_{1D} = 3.01 \pm 0.11$ km s^{-1}has been adopted and NGC 2100 has therefore been shown to be in virial equilibrium. This adds evidence to the theory that young star clusters appear to remain in virial equilibrium from an early age and hence expand owing to stellar evolution on a relatively slow timescale (10 Myr Portegies Zwart et al. 2010). We compare the velocity dispersion profile estimated here to that of other young massive clusters in the LMC and the Galaxy and find that the distribution of velocity dispersions is consistent with this expansion.

Characterisation of the velocity dispersion profile for the cluster allows for the first time the dynamical mass to be estimated (assuming virial equilibrium) as $log(M_{dyn}/M_\odot) > 4.8$. A discussion of the appropriate value of η for this cluster is detailed in Section 3.3.

We estimate stellar parameters for the RSGs in NGC 2100 using the J-band analysis technique (Davies et al. 2010) for all targets within the sample. We find the average metallicity for RSGs in NGC 2100 is $-0.30 \pm 0.11\,dex$, which agrees well with previous studies within this cluster. We construct a H-R diagram of RSGs within NGC 2100 and estimate the age of the cluster using isochrones fitting (Ekström et al. 2012; Georgy et al. 2013) to be 20 ± 5 Myr, in good

agreement with previous estimate of this cluster (Niederhofer et al. 2015).

ACKNOWLEDGEMENTS

...

REFERENCES

Andrews, P. J., & Lloyd Evans, T. 1972, MNRAS, 159, 445

Bergemann, M., Kudritzki, R.-P., Plez, B., et al. 2012, ApJ, 751, 156

Bergemann, M., Kudritzki, R.-P., Würl, M., et al. 2013, ApJ, 764, 115

Bergemann, M., Kudritzki, R.-P., Gazak, Z., Davies, B., & Plez, B. 2015, ApJ, 804, 113

Clark, J. S., Negueruela, I., Crowther, P. A., & Goodwin, S. P. 2005, A&A, 434, 949

Crowther, P. A., Schnurr, O., Hirschi, R., et al. 2010, MN-RAS, 408, 731

Davies, B., Figer, D. F., Kudritzki, R.-P., et al. 2007, ApJ, 671, 781

Davies, B., Origlia, L., Kudritzki, R.-P., et al. 2009, ApJ, 696, 2014

Davies, B., Kudritzki, R.-P., & Figer, D. F. 2010, MNRAS, 407, 1203

Davies, B., Kudritzki, R.-P., Plez, B., et al. 2013, ApJ, 767, 3

Davies, B., Kudritzki, R.-P., Gazak, Z., et al. 2015, ApJ, 806, 21

Davies, R. I., Agudo Berbel, A., Wiezorrek, E., et al. 2013, A&A, 558, A56

de Koter, A., Heap, S. R., & Hubeny, I. 1998, ApJ, 509, 879

Ekström, S., Georgy, C., Eggenberger, P., et al. 2012, A&A, 537, A146

Eldridge, J. J., Izzard, R. G., & Tout, C. A. 2008, MNRAS, 384, 1109

Elson, R. A. W. 1991, ApJS, 76, 185

Evans, C. J., Lennon, D. J., Smartt, S. J., & Trundle, C. 2006, A&A, 456, 623

Evans, C. J., Taylor, W. D., Hénault-Brunet, V., et al. 2011, A&A, 530, A108

Evans, C. J., van Loon, J. T., Hainich, R., & Bailey, M. 2015, arXiv:1508.03490

Ford, H., 1970, PhD. Thesis, University of Wisconsin.

Freeman, K. C., Illingworth, G., & Oemler, A., Jr. 1983, ApJ, 272, 488

Gazak, J. Z., Bastian, N., Kudritzki, R.-P., et al. 2013, MNRAS, 430, L35

Gazak, J. Z., Davies, B., Kudritzki, R., Bergemann, M., & Plez, B. 2014, ApJ, 788, 58

Gazak, J. Z., Davies, B., Bastian, N., et al. 2014, ApJ, 787, 142

Gazak, J. Z., Kudritzki, R., Evans, C., et al. 2015, ApJ, 805, 182

Georgy, C., Ekström, S., Eggenberger, P., et al. 2013, A&A, 558, A103

Gieles, M., Sana, H., & Portegies Zwart, S. F. 2010, MN-RAS, 402, 1750

Gratton, R. G., Lucatello, S., Carretta, E., et al. 2012, A&A, 539, A19

Gustafsson, B., Edvardsson, B., Eriksson, K., et al. 2008, A&A, 486, 951

Hénault-Brunet, V., Evans, C. J., Sana, H., et al. 2012, A&A, 546, A73

Jasniewicz, G., & Thevenin, F. 1994, A&A, 282, 717

King, I. R. 1966, AJ, 71, 64

Lada, C. J., & Lada, E. A. 2003, ARA&A, 41, 57

Lapenna, E., Origlia, L., Mucciarelli, A., et al. 2015, ApJ, 798, 23

Longmore, S. N., Kruijssen, J. M. D., Bastian, N., et al. 2014, Protostars and Planets VI, 291

Massey, P., & Hunter, D. A. 1998, ApJ, 493, 180

McConnachie, A. W. 2012, AJ, 144, 4

McLaughlin, D. E., & van der Marel, R. P. 2005, ApJS, 161, 304

Miller, B. W., Whitmore, B. C., Schweizer, F., & Fall, S. M. 1997, AJ, 114, 2381

Niederhofer, F., Hilker, M., Bastian, N., & Silva-Villa, E. 2015, A&A, 575, A62

Patrick, L. R., Evans, C. J., Davies, B., et al. 2015, ApJ, 803, 14

Points, S. D., Chu, Y. H., Kim, S., et al. 1999, ApJ, 518, 298

Portegies Zwart, S. F., McMillan, S. L. W., & Gieles, M. 2010, ARA&A, 48, 431

Robertson, J. W. 1974, A&AS, 15, 261

Smith, M. G., & Weedman, D. W. 1971, ApJ, 169, 271

Whitmore, B. C., & Schweizer, F. 1995, AJ, 109, 960

Zepf, S. E., Ashman, K. M., English, J., Freeman, K. C., & Sharples, R. M. 1999, AJ, 118, 752